Cement and Concrete Research 39 (2009) 1139–1148

Contents lists available at ScienceDirect

Cement and Concrete Research

journal homepage: http://ees.elsevier.com/CEMCON/default.asp

Experimental evidence of a moisture clog effect in cement-based materials under temperature

Xiao-Ting Chen [a], Th. Rougelot [b], C.A. Davy [a,*], Wei Chen [a], F. Agostini [a], F. Skoczylas [a], X. Bourbon [c]

[a] Laboratoire de Mécanique de Lille (LML), UMR 8107, and Ecole Centrale de Lille, BP 48, F-59651 Villeneuve d'Ascq Cedex, France
[b] Laboratoire de Mécanique de Lille (LML), UMR 8107, and Polytech'Lille, Bd P. Langevin, F-59650 Villeneuve d'Ascq, France
[c] Andra, 1-7 rue Jean Monnet, F-92298 Châtenay-Malabry Cedex, France

ARTICLE INFO

Article history:
Received 11 July 2008
Accepted 20 July 2009

Keywords:
Permeability
Moisture clog
Temperature
Saturation level
Scale effect

ABSTRACT

This study is an original contribution to the understanding of the hydraulic behaviour of cement-based materials when subjected to temperature rises. Permeability is measured *continuously during heating* by injecting inert gas into a sample at homogeneous temperature. Using a confining cell especially designed in our laboratory, the sample is submitted to a constant heating rate, up to 200 °C, superimposed to hydrostatic pressure (at ca. 5 MPa). In parallel with a normalised CEM II mortar (water-to-cement ratio (W/C) of 0.5), a CEM V-cement-based concrete, used in nuclear waste storage applications, is studied. For normalised mortar, gas retention is evidenced, depending on the sample size (scale effect), water saturation level S_w, and heating rate. For dry normalised mortar, permeability may be divided by two during heating. In conjunction with thermo-gravimetry analysis (TGA) results, such evolution is attributed to the dehydration of C–S–H around 150 °C. Indeed, mass loss after heat cycling is substantially higher than that due to free water release solely: mortar loses structural, bound water during the process. For partially-saturated and long mortar samples, a gas retention phenomenon is recorded when heating at a rate of ca. 4.9 °C/min. Our analysis is that free water inside the macropores, as well as bound water released from the C–S–H, dilates or vaporizes, and obstructs the interconnected porous network. Due to moisture clogging, no more gas is allowed through the material pore network: a so-called *gas retention phenomenon* occurs. Most interestingly, although loosing structural water like normalised mortar, yet over a wider temperature range, dry CEM V concrete displays good temperature resistance, as its permeability remains constant during heating. For highly partially-saturated concrete, a gas retention effect is recorded. As a conclusion, observed phenomena at the laboratory scale testify of potentially strong gas retention effects upon engineering structures subjected to temperature gradients over time. Indeed, quite low temperature rises (and heating rates) are able to induce moisture clogging inside partially-saturated materials. It is also concluded that cement-based material composition, i.e. bound water release ability, is influential in gas transport phenomena under temperature.

1. Introduction

In the Civil Engineering area, concrete structures may be subjected to unexpected high temperature rises, such as during fire accidents inside tunnels [1,2] or buildings, which may have dramatic consequences on the economic or even human grounds. Nuclear reactor structures [3] and nuclear waste disposals also require extensive use of cement-based materials. These may be subjected to temperature rises as high as 250 °C in nuclear reactor vessels [4,5], or rather 100 °C for nuclear waste storage, due to a long-lasting nuclear material activity. In such applications, cement-based materials must provide proper fluid confinement, even in the case of inner pressure build-up [6].

Macroscopic phenomena related to concrete behaviour and degradation under temperature have been extensively investigated [2,7–11]. At the material level, high temperatures (above 100 °C) affect irreversibly both elastic stiffness and material strength, those being the signature, respectively, of thermal damage and thermal decohesion [2,12]. Under temperature, crack initiation is generally attributed to varied phenomena [8,13,14], and in particular to increasing mismatch of dilation/shrinkage between paste and aggregates, rigidity differences between cement paste and aggregates, strength-weakening decomposition of cement paste hydrates, and dehydration-induced cracks, the latter being attributed to thermal mismatch of dilation/shrinkage among the different cement paste hydration products [1].

At the structural level, the degradation of concrete exposed to high temperature may lead to *spalling* i.e. to a brittle fracture of the heated material surface [1,15]. This is more pronounced for high performance concretes (HPCs) than for ordinary concretes (OCs), due to the former

* Corresponding author. Tel.: +33 3 20 33 53 62; fax: +33 3 20 33 53 52.
E-mail address: catherine.davy@ec-lille.fr (C.A. Davy).

0008-8846/$ – see front matter © 2009 Elsevier Ltd. All rights reserved.
doi:10.1016/j.cemconres.2009.07.015

higher brittleness and also to the differences in pore structure resulting from differences in mix designs, the solid matrix in HPCs being usually denser than that of an OC. These may lead to complete failure of the concrete structure [16]. As mentioned by Ulm et al. [2], most authors agree that spalling results mainly from two physical processes: (1) gas pressure build-up inside the porous network [16,17], and (2) restrained thermal dilation close to the heated surface [3]. While pore pressure build-up triggers crack formation, crack propagation and spalling rather result from thermal stresses release. According to Bažant [3], potential energy release of compressive thermal stresses occurs, whereas Anderberg [16] accounts, as the main failure cause, for tensile stresses generated by two- or three-dimensional thermal stress field distribution. More recently, Ulm et al. [2] and Msaad [11] describe failure initiation as due to a combination of compressive thermal stresses and tensile stresses (generated by pore pressure increase) using the Willam-Warnke yield criterion [18].

While it is essential to avoid spalling and complete collapse of concrete structures, it is also vital to avoid radioactive fluid leakage from concrete vessels or waste packages. In particular, hydrogen gas may be produced within a nuclear waste storage tunnel, due to radioactive waste decay, water radiolysis and humid corrosion [19]. In such cases, gas permeability evolution with temperature is a key parameter [17]: low transport capabilities (i.e. proper radioactive fluid confinement) may be assessed, as well as any tendency to pore pressure build-up (i.e. assessment of potential spalling initiation).

At the microstructural scale of a cement-based porous material, heating first results in free water drainage (i.e. water situated in the macropores), and, from 90 °C onwards [20], in bound water drainage, both stages being combined with pore network dilation (or shrinkage) and even possible micro-cracking [21–23]. Despite micro-cracking, relative gas permeability may become zero in some areas [17], meaning that no gas is able to flow through the interconnected pore network: a so-called *gas retention phenomenon* occurs within the pore network. On the whole, combined effects of pore size variation, liquid water dilation, water vapour formation or condensation, may induce pore pressure build-up. This effect is emphasized whenever gas is forced to flow through the material, so that a gas retention phenomenon, also called *moisture clog effect* occurs [15].

In particular, pore pressure build-up is increased by high moisture content, concrete density (essentially for HPCs), external compressive stress state, and rapid temperature rise [16]. The lower the initial permeability, the sooner a moisture clog is generated and the higher the pressure build-up appears [15,17].

Complementarily to existing modeling investigations [2,4,7,10,11], this study aims at identifying *experimentally* upon which conditions the advent and duration of a moisture clog effect depends in presence of a gas flow. While Kalifa et al. [17] impose a huge spatial temperature gradient to a prismatic *oven-dried* concrete specimen (i.e. 800 °C on one face of a 12 cm thick sample), the whole volume of our initially dry or partially-saturated specimen remains at a homogeneous temperature throughout the heat cycling test [24]. The sample is subjected to a heating/cooling cycle at constant heating rate, simultaneously to hydrostatic stress, in order to reproduce simplified *in situ* loading conditions, e.g. in a nuclear material container mass. Hydrostatic stress, at sufficiently high level as used here, also tends to close existing micro-cracks and avoids opening any other. Heating rate is varied only from 1 cycle to the other. A quasi-stationary inert gas flow passes through the sample as well, and gas permeability is recorded *continuously* during heating. In the literature, see [25], permeability identification with increasing temperature is available, yet by using water and up to 100 °C only, so that potential interactions with the interstitial fluid may occur, which the use of gas avoids. M. Lion et al. [21] have used almost the same experimental set-up as ours. However, their gas permeability measurements were performed at three stabilised temperature levels only (at 25, 105 and 200 °C, each maintained for at least 8 h) under constant confinement, without sample temperature recording, and on an initially *dry* normalised mortar ($w/c = 0.5$). Permeability appeared to remain almost constant up to 105 °C, whereas it increased significantly at 200 °C. As gas permeability was not measured continuously, no decrease in permeability, which could indicate the onset of a gas retention phenomenon, was ever observed. Similar results are obtained by M. Choinska [26] upon a uniaxially-loaded dry concrete used in nuclear reactor confinement vessels, after up to 60 h temperature stabilisation, and up to 150 °C. Nevertheless, preliminary studies by L. Montigny [27] have shown a permeability decrease when heating up to 205 °C a dry industrial concrete sample, in the first few hours *before* temperature stabilisation.

The originality of the present contribution consists in evidencing the moisture clog phenomenon through *continuous* gas permeability measurements during heating, along with material temperature recording. We also account for the influence of scale, *saturation level* S_w, heating rate and cement-based material composition. Complementarily, thermogravimetry analysis highlights the cement paste microstructural modifications with heating, which explain, for some part, gas permeability steadiness or decrease.

2. Theory

2.1. Gas permeability identification under quasi-stationary gas flow and isothermal conditions

The gas permeability measurement technique developed in our laboratory for low permeability ranges (below 10^{-15} m^2) has been extensively described in [6,28]. In brief, a cement-based material circular cylindrical sample is placed inside a triaxial cell at given hydrostatic pressure P_c, and it is subjected to a stationary inert gas flow along its height (axis $\vec{x}$), see Fig. 1. Average gas volume flowrate Q_v is assessed by measuring the time Δt required to get a small pressure decrease ΔP of chosen value, on the sample upstream side. This is performed by closing the valve situated upstream of the buffer reservoir and of the sample. By assuming quasi-static flow and perfect gas state equation, Q_v writes:

$$Q_v = \frac{V_r \Delta P}{P_{mean} \Delta t} \tag{1}$$

where V_r is the buffer reservoir volume, gas pressure is P_1 on the sample upstream side, $P_0 = P_{atm}$ on its downstream side and P_{mean} is the average upstream gas pressure: $P_{mean} = P_1 - (\Delta P/2)$. Pipes volume is considered negligible compared to V_r. In the following, $P_1 = 1.4$ to 1.5 MPa and ΔP varies between 0.05 and 0.1 MPa.

Permeability K_x along sample height L is given by Darcy's law, mass conservation and perfect gas state equation as:

$$K_x = \frac{\mu Q_v}{A} \frac{2LP_{mean}}{(P_{mean}^2 - P_0^2)} \tag{2}$$

where μ is gas viscosity. It is taken as 2.2×10^{-5} Pa s at 20 °C for argon. Eq. (2) provides apparent gas permeability. This means that K_x may also incorporate gas molecule slippage along pore surfaces, i.e. Klinkenberg effect, see Section 3.

2.2. Gas permeability identification under quasi-stationary gas flow and non-isothermal conditions

All our tests are conducted *during* temperature increases of up to 200 °C. Our methodology for evaluating K_x remains identical to isothermal conditions, yet gas viscosity μ and volume flowrate Q_v are corrected. Indeed, the injected gas, although coming from a buffer reservoir at 20 °C, is subjected to a temperature increase $(T - T_0)$ when passing through the triaxial cell and through the sample which

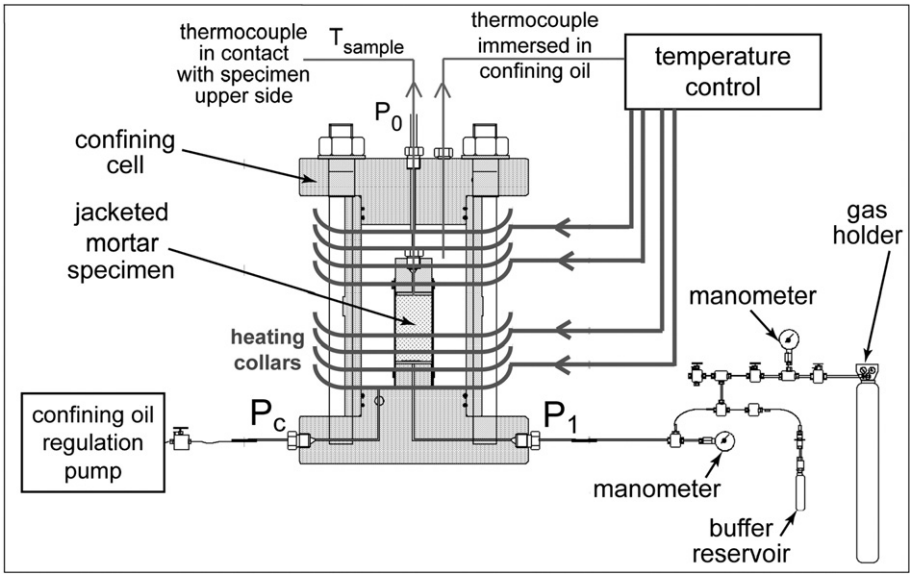

Fig. 1. Experimental set-up used for continuous gas permeability tests under confinement and with increasing temperature (of up to 200 °C).

is at uniform temperature T. This is mainly accounted for by adapting gas viscosity to the current temperature T inside the sample according to:

$$\mu(T) = \mu(T_0)\left(\frac{T}{T_0}\right)^{0.72} \text{with} T_0 = 300\,\text{K}(=\ 27^{\circ}C) \tag{3}$$

where T is expressed in kelvin and $\mu(T_0) = 2.283 \times 10^{-5}$ Pa s, see [29].

However, the porous solid may be partially water-saturated so that heating up to 200 °C will induce free water vaporization, or it may lose bound (structural) water. With increasing temperature, argon gas flowing through the sample gets mixed with more and more vaporized water, so that this phenomenon potentially alters the flowing gas mix viscosity. Argon viscosity [29] varies between

$$\mu_{\text{argon}}(T_0 = 27^{\circ}\text{C}) = 2.283 \times 10^{-5}\ \text{Pa s}$$

and

$$\mu_{\text{argon}}(T = 200^{\circ}\text{C}) = 3.05 \times 10^{-5}\ \text{Pa s},$$

while water vapour viscosity [29] varies between

$$\mu_{\textit{Water vapour}}(T = 100^{\circ}\text{C}) = 1.25 \times 10^{-5}\ \text{Pa s}$$

and

$$\mu_{\textit{Water vapour}}(T = 200^{\circ}\text{C}) = 1.62 \times 10^{-5}\ \text{Pa s}$$

so that both are of the same order of magnitude. Finally, as water vapour proportion in the gas mix is unknown whatever the temperature above 100 °C, we have chosen to take into account only the main flowing gas (namely argon) for gas permeability assessment, given that both water vapour and argon have similar viscosities.

The second main modification is related to gas density variation with temperature $\rho(T)$.

Inside the reservoir constant volume V_r, temperature is assumed constant at T_0 throughout the test, so that mass variation Δm inside the reservoir during time Δt writes:

$$\Delta m = Q_m \Delta t = \Delta\rho V_r \tag{4}$$

$\Delta\rho$ is the gas density variation due to mass flow throughout the reservoir. Simultaneously, gas pressure inside the reservoir decreases by ΔP during Δt, with ΔP lower by one (or two) orders of magnitude than the average gas pressure P_{mean} evaluated during Δt: $\Delta P \ll P_{mean}$. At constant temperature T_0, the perfect gas assumption provides:

$$\frac{\Delta P}{P_{mean}} = \frac{\Delta\rho}{\rho_{mean}(T_0)} \tag{5}$$

where $\rho_{mean}(T_0)$ is the average gas density at T_0, evaluated during Δt. Eqs. (4) and (5) provide mass flow rate $Q_m(T_0)$ at the buffer reservoir exit as:

$$Q_m(T_0) = \frac{\Delta P\, \rho_{mean}(T_0)}{P_{mean}\Delta t} V_r. \tag{6}$$

Gas flows from the buffer reservoir down to the sample, which is at constant temperature T. Gas mass conservation between the buffer reservoir exit (at temperature T_0) and the sample upstream side (at temperature T) imposes mass flow rate conservation, so that $Q_m(T_0) = Q_m(T) = Q_m$. Mass flow rate Q_m is related to volume flowrate $Q_v(T)$ by: $Q_m = Q_v(T)\rho(T)$. Moreover, no pressure decrease is assumed to occur between the buffer reservoir exit and the sample upstream side, so that the latter is at constant pressure P_{mean}, and the perfect gas state equation writes there $\rho(T) = \frac{T_0}{T}\rho_{mean}(T_0)$. Finally:

$$Q_v(T) = \frac{T}{T_0}\frac{V_r\ \Delta P}{P_{mean}\ \Delta t} \tag{7}$$

Eqs. (2), (3) and (7) finally provide $K_x(T)$ by replacing Q_v with $Q_v(T)$ and μ with $\mu(T)$.

2.3. Klinkenberg effect

While fluid viscosity is accounted for by Darcy's law, Klinkenberg effect accounts for gas slippage along porous network surfaces. This phenomenon is at the origin of a lower apparent permeability K_{app} with increasing gas pressure than the real (or intrinsic) material permeability K_{int}: $K_{app} = K_{int}(1 + \beta/P_m)$, where $P_m = (P_0 + P_1)/2$ is the average gas pressure through the sample ($P_m \neq P_{mean}$).

In this study, most samples are partially-saturated i.e. partially-filled with liquid water or water vapour, and otherwise, the dehydration of cement paste phases with increasing temperature adds water vapour through the porous network. Therefore, an accurate evaluation of the Klinkenberg effect appears difficult, for it would account for several combined phenomena, such as slippage at the

solid pore surface and at the liquid water surface, pore obstruction due to liquid water presence, etc. For initially dry samples, Lion et al. [21] have used long stabilisation times (8 h at least) at a constant given temperature, so as to ensure that all water is removed from the sample, prior to performing gas permeability tests and deducing intrinsic permeability K_{int} and Klinkenberg coefficient β. As this study aims rather at identifying the moisture clog effect, Klinkenberg effect assessment (and long stabilisation times at constant temperature) have not been performed.

2.4. Relative permeability vs. absolute permeability

Due to the presence of several fluids (liquid water/water vapour/argon gas) mixed together inside the porous network, gas permeability measurements are rather *relative* permeability evaluations than intrinsic and absolute ones, as represented by the classical petrophysical two-phase flow theory [30]. Nevertheless, for the sake of simplicity, it is assumed in the following, that gas relative permeability assessment method is not influenced by water presence, i.e. water and gas flow are assumed uncoupled.

3. Experimental methodology

3.1. Materials

A normalised mortar with a water-to-cement ratio (W/C) of 0.5 has been made using normalised sand (from Leucate, France) and Type II Portland cement referenced CEM II/B-M (LL-S) 32.5R. European Standard EN 197-1/2000 describes this cement composition as comprising 65–79% clinker, 21–35% calcite and 0–5% of secondary constituents. This mortar is used for a wide variety of studies in our laboratory, see for instance [31–35], and it may be easily reproduced by other laboratories for comparison and/or further studies. Ulm et al. [36] use a very similar (W/C) = 0.5 model mortar, except that it is composed of Type I Portland cement. On average, our mortar porosity ϕ_0 is of 12.9% ± 0.1, as evaluated by the ethanol saturation method, while MIP measurements provide ϕ_0 = 13.4%.

Industrial concrete with a water-to-cement (W/C) ratio of 0.48 is also considered. It is studied in nuclear waste storage experimental facilities by Andra (French Agency for Nuclear Waste Management) [6,37]. This concrete is composed of Type V cement (referenced CEM V/A), sand (0 to 4 mm), gravel limestone (5 to 12 mm) and of a proportion of super-plasticizer, aimed at reducing water need and representing 2.5% of the cement mass (i.e. SP/C = 0.025). CEM V/A cement comprises 60% clinker in mass, 22% blast-furnace slag, 14% siliceous filler (i.e. fly ash) and 4% setting regulator, in compliance with NF EN 196-4 European Standard. Concrete porosity is evaluated by the water saturation method at 14.2% ± 0.5, which is only 1% higher than our normalised mortar. For radial gas permeability assessment, M. Choinska [26] uses comparable concrete, made of calcareous aggregates, CEM II/A cement and Glenium 21 super plasticizer.

All samples are cored to 37 mm diameter, and cut to either short length (ca. 35 mm) or long length (ca. 70 mm) in order to vary their length-to-diameter ratio from about 0.9 to 1.8, see Table 1. Reference dry material state is taken after oven-heating at 60 °C until constant weight, in accordance with former experimental work performed in our laboratory [21,31]. Such curing conditions aim at allowing evaporation of free water from the macropores, without significant effect upon calcium silicate hydrates (C–S–H) gel.

Alternately, samples have been partially-saturated, from an initial fully water-saturated state, by placing them in an hermetic chamber at 59.1% uniform relative humidity (RH) at 20 °C, using a NaBr salt solution [28]. Partial saturation S_w is defined as:

$$S_w(\%) = \frac{m_{60\%} - m_{dry}}{m_{sat.} - m_{dry}} \times 100 \quad (8)$$

where $m_{60\%}$ is the specimen mass when placed inside the RH-controlled chamber, $m_{sat.}$ is the 100% water-saturated sample mass (initial state). Samples used in this study have not been directly dried to evaluate their dry mass m_{dry}. Rather, additional 37 mm-diameter and 70 mm-length samples have been oven-dried at 60 °C until mass stabilisation, and then weighed: mass loss $m_{sat.} - m_{dry}$ represents 7.0 ± 0.2% of fully water-saturated mass $m_{sat.}$ for CEM II mortar, and 5.8 ± 0.2% for CEM V concrete. For mortar, S_w ranges from 44.7% for long sample No. 16 to 53.4% for long sample No. 17, see Table 1. It is to be noted here that the 59%RH-controlled curing has been kept for 6 months for sample No. 16, while sample No. 17 and sample No. 26 have been cured for 3 months only, so that their initial saturation rate S_w is higher. Yet mass loss rates are similar, and very low for all samples: mass loss is of ca. 7 mg/day for mortar sample No. 16 after 6 months curing, whereas samples No. 17 and No. 26 lose mass at a rate of 3 mg/day or 7 mg/day respectively after 3 months curing. Concrete samples are either dry (CEMV No. 1) or quite heavily partially-saturated (CEMV No. 2) with $S_w \approx 80\%$, see Table 1.

3.2. Experimental procedures

3.2.1. Permeability devices and measurement accuracy

Our triaxial cell, see Fig. 1, provides hydrostatic loading to the sample by pressurizing hydraulic oil around it. Hydraulic oil is selected so as to support both confinement at a constant pressure of 5.4 MPa ± 0.2 and heating up to 200 °C without major viscosity or state changes. Temperature is applied progressively to the oil using heating collars placed around the triaxial cell shaft. Collar and oil temperatures are controlled throughout the tests using a regulating system which takes temperature values from thermocouples placed inside the oil and upon the collars. The triaxial cell is thermally-insulated in order to limit heat loss. A K-type thermocouple passes through the triaxial cell outlet pipe, so as to provide temperature of the specimen upper side, with an accuracy of ±0.1 °C. Every second, upstream gas pressure P_1, and hence ΔP, are recorded using a Kobold^{TM} manometer (full range 0–2.5 MPa) with an accuracy of 2.5 kPa (i.e. 0.1% of the full range).

Table 1
Sample length-to-diameter ratios, partial saturation S_w and mass loss Δm after all three heating cycles.

Sample	No. 23	No. 16	No. 17	No. 26	CEMV No. 1	CEMV No. 2
Material	Mortar				Concrete	
Length-to-diameter ratio	1.85	1.85	1.86	0.92	1.6	1.6
Porosity ϕ_0 (%)	12.9				14.2	
Curing conditions	Dry	6 months at 60% RH	3 months at 60% RH	3 months at 60% RH	Dry	3 months at 60% RH
Initial water saturation level S_w (%)	0	44.7	53.4	50.8	0	79.6
Free water mass before heat cycling (g)	0	5.67	6.83	3.33	0	7.36
Sample mass loss Δm (g)	3.66	8.93	10.68	3.64	0.40	7.33
(% initial mass)	(−2.2%)	(−5.1%)	(−6.0%)	(−4.1%)	(−0.3%)	(−4.6%)
Final water saturation level S_w (%)	0	0	0	0	0	≈0

3.2.2. Heating rates

For each sample, *three successive heating cycles* (20 °C→T_{max}→20 °C) have been imposed with increasing target temperatures T_{max} of 60, 105 and 200 °C. Those have been set using the oil heat-regulation system (see Section 1), and cooling is performed down back to 20 °C by simply stopping collar heating after about 2 h stabilisation at target temperature. Sample temperature evolution vs. time is derived and provides maximum heating rate values of 1.41 ± 0.10, 2.49 ± 0.05 and 4.91 ± 0.35 °C/min during the stationary heating phase, for each of the three target temperatures respectively, see Table 2. Such heating rates are in the low range compared to those encountered during fire accidents of concrete structures, see [2].

Temperature homogeneity inside the sample during heating has been checked through a preliminary test, see [24]. A 65 mm diameter and 50 mm height concrete sample has been equipped with five thermocouples, three close to its surface and two in its bulk, and has been subjected to three heating cycles (20 °C→T_{max}→20 °C) up to T_{max} = 50, 90 °C and 130 °C successively. Results show homogeneous temperatures inside the sample, with only very small temperature differences representing 0.25 °C at most between bulk and surface. Oil and concrete average temperatures display greater difference: this difference is of 3.75 °C after 2 h 45 min, when stabilisation at target temperature 90 °C is reached.

3.2.3. Thermo-gravimetry analysis (TGA)

After drying at 60 °C until mass stabilisation, 150 to 300 mg powdered or block mortar (or concrete) samples have been placed and heated continuously inside a SETARAM^{TM} microscale up to 800 °C at a constant heating rate of 200 °C/h. Concrete samples have been taken aside large aggregates so that the sample mass m is assumed solely composed of cement, water and super plasticizer: $m = C + W + SP$. The heating method is labelled as *dynamic* because no temperature stabilisation is performed when a decomposition (i.e. chemical reaction) begins [20]. Sample mass and temperature are recorded regularly (f = 1 Hz) from the microscale and from a K-type thermocouple placed beside the sample. Mass loss is expressed in percentage of the sample cement mass as:

$$\%m = 100\{1-\{((m(t)-m_0)*(1 + W/C + SP/C))/m_0\}\},$$

where m_0 is sample initial mass, $m(t)$ is sample mass at time t, W/C is water-to-cement ratio, and SP/C is super plasticizer-to-cement ratio. W/C is equal to 0.5 for mortar and 0.48 for concrete; SP/C is equal to zero for mortar and to 0.025 for CEMV concrete. Normalising mass loss by the cement mass allows comparing directly mass losses between different cement paste compositions, i.e. here between normalised mortar and CEMV concrete. Moreover, $\frac{d\%m}{dt}$ thermo-gravimetry derivative (or TGD) is computed analytically from the Naradaya–Watson estimate of %m, which is a kernel smoother, and corresponds to a signal processing method detailed in [38]. The micro-scale drift with temperature is recorded through a test on a pure gold sheet sample; it is subtracted from any record upon cement-based materials.

4. Results and analysis

4.1. TGA results

As explained in [20,39] and evidenced in [40], the different phases present in a cement paste, i.e. mainly C–S–H (and aluminates), then (with decreasing proportion) portlandite, calcite, and ettringite, decompose during quite distinct temperature ranges when cement paste is subjected to heating. A general agreement about those temperature ranges is as follows [20]. Mortar is assumed subjected to a constant heating rate up to 800–1000 °C (dynamic method). After free water release up to around 100 °C, C–S–H (and aluminates) decompose from 105 °C (or 145 °C according to some authors [20]) and up to 400 °C; portlandite $Ca(OH)_2$ releases its water molecule from 400 °C to 600 °C; calcite $CaCO_3$ releases a CO_2 molecule from 600 °C and up to 800–1000 °C. When present in dry cement paste, ettringite decomposition starts between 70 and 75 °C [40]. It leads to monosulfoaluminate formation, which in turn, leads to hydrogarnet and anhydrite formation above 85–90 °C [41,42]. It is to be noted that these temperatures are notably modified in presence of liquid water [20,43].

In practice, the cement-based material is oven dried at 60 °C until mass stabilisation (i.e. it is considered *fully dried*), cut to small blocks, or powdered, and then placed inside the TG apparatus. After possible free water release (or ettringite decomposition) at the heating onset, roughly up to 105 or 145 °C, further water (or carbon dioxide) release is assumed to be due to cement paste phases decomposition solely. Complementarily, mass loss derivative peaks define the actual temperature ranges during which the main chemical reactions (i.e. decompositions) occur.

For mortar, see Fig. 2(a), three significant mass loss derivative peaks are as expected: one main decomposition, attributed to C–S–H occurs at 150 °C, more exactly between 90 °C and 240 °C; $Ca(OH)_2$ dehydration is around 440–450 °C, and calcite $CaCO_3$ decarboxylation is at 700–730 °C. Test No. 1 corresponds to lesser mass loss than Test No. 2, the former been performed on small blocks, and the latter on powdered material: the higher the material surface, the greater its mass loss.

For CEM V concrete, see Fig. 2(b), very close results are obtained from both tests upon powdered samples, and mass loss up at 400 °C is slightly lower (by 7%) than that of powdered mortar, at a value of 6.7% ± 0.1% for mortar and 6.2% ± 0.1% for concrete. Yet, a significant difference exists between concrete and normalised mortar TGA results: for concrete, bound water loss above 105 °C spans over a much wider range than for mortar. In particular, at 200 °C, where our gas permeability measurements under hydrostatic loading end, 3.3% ± 0.1% cement mass have been lost by mortar, whereas concrete has released 2.7% ± 0.3% cement mass only, which is lower than mortar by 18%. Indeed, C–S–H decomposition is associated to several smaller mass loss derivative peaks than for mortar, see Fig. 2(b). This is interpreted as being due to differences of hydration and composition of the C–S–H, between CEM II mortar and CEM V concrete. Indeed, for normalised CEM II mortar, the single mass loss derivative peak for C–S–H decomposition may be associated to a single C–S–H stoichiometry, and its amplitude is associated to reasonable bound water release. On the opposite, fly ash and blast furnace slag in CEM V

Table 2
Maximum heating rates are given for each sample and cycle, respectively up to 60, 105 and 200 °C.

Maximum heating rate (°C/min)	No. 23	No. 16	No. 17	No. 26	CEMV No. 1	CEMV No. 2	Average value (°C/min)
Cycle 1 (20 °C→60 °C→20 °C)	1.44	1.23	1.47	1.32	1.41	1.57	1.41 ± 6.2%
Cycle 2 (20 °C→105 °C→20 °C)	2.44	2.43	2.40	2.35	2.65	2.67	2.49 ± 4.5%
Cycle 3 (20 °C→200 °C→20 °C)	4.63	4.53	4.85	5.14	5.20	5.12	4.91 ± 4.9%

Each cycle has been successively applied to each mortar sample Nos. 16, 17, 23 and 26, and to concrete samples CEM V Nos.1 and 2. Average values and associated absolute variation to the average (expressed in percentage of the average) are also provided.

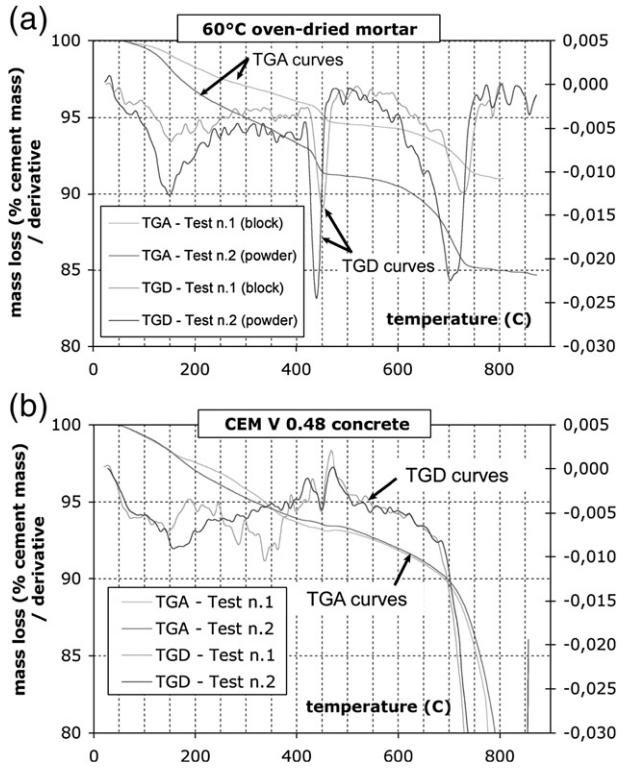

Fig. 2. TGA test results for (a): 60 °C oven-dried normalised mortar. The three main mass loss derivative peaks correspond to the decomposition of C–S–H, $Ca(OH)_2$, and calcite $CaCO_3$ respectively, with increasing temperature. (b): CEMV (w/c) = 0.48 concrete. In both cases, mass loss derivatives are magnified 300×. Test results of two different samples are represented for each material.

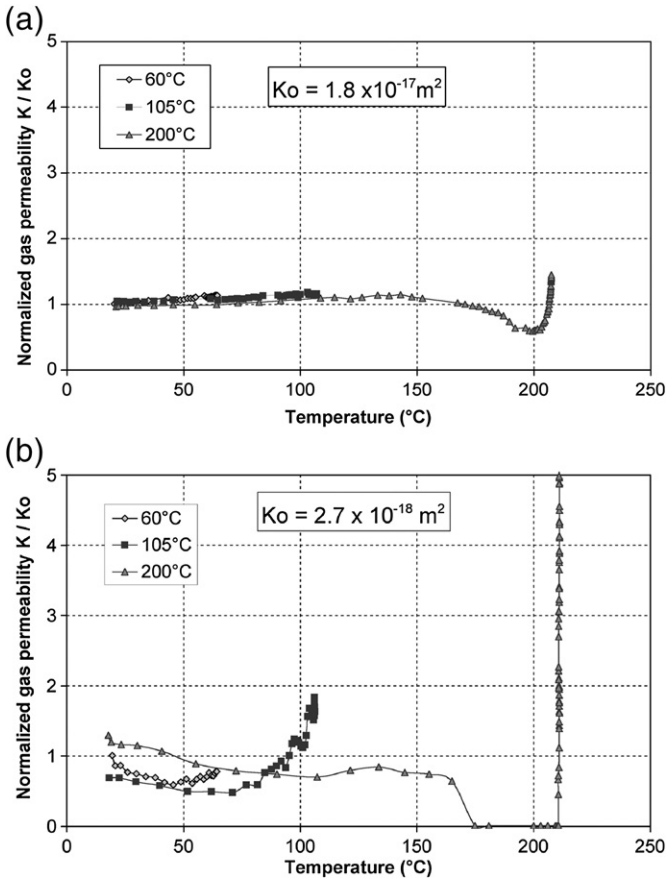

Fig. 3. Effect of the initial saturation rate for long mortar samples (a): Dry sample No. 23; (b): Partially-saturated (Sw = 44.7%) sample No. 16. Initial apparent gas permeability K_o is also given.

concrete induce several mass loss derivative peaks, i.e. a more varied C–S–H stoichiometry. Moreover, these peaks are of small amplitude and each associated mass loss also is, so that less water is released at a given temperature by the CEM V concrete C–S–H phases, although the total mass loss between 105 and 400 °C is similar for both mortar and concrete.

According to C–S–H molecular structure, water content of a C–S–H phase is closely linked to its calcium-to-silica (C/S) ratio. In the literature, stoichiometry assessment of natural C–S–H and hydrated cement observations show that water stoichiometry decreases with (C/S) ratio [44–46].

Ordinary Portland cement hydration leads to high portlandite amounts in relation to a (C/S) ratio over 1.5–1.7 [45,46]. The presence of mineral additions such as slag or fly ashes in blended cements such as CEM V promote pozzolanic reactions and consume portlandite as well as free or bound water, in order to form C–S–H phases with lower (C/S ratio) than in pure Portland cements. As the (C/S) ratio is lower, the pozzolanic reaction engages a water reaction process. As a result, water is bound more closely to the structure. It is then more difficult to dehydrate C–S–H compounds and release water from those solid phases. In brief, less water is bound per C–S–H chemical formula, i.e. less water is lost by each C–S–H between 145 and 400 °C than with normalised CEM II mortar, although both lose globally equivalent water amounts, as displayed in Fig. 2(a) and (b): water loss is much more *progressive* for CEMV concrete than for CEMII mortar. This is in favour of better gas transport abilities for CEMV concrete than CEM II mortar when subjected to heating. This is thought to explain the steadiness of dry CEMV concrete gas permeability with temperature up to 200 °C, see Fig. 6(a), whereas dry mortar displays a clear permeability decrease above 150 °C, see Fig. 3(a). Similarly, as the absence of significant mass loss derivative peak between 400 and 600 °C testifies, CEM V composition does not allow portlandite formation, because the pozzolanic reaction transforms portlandite into C–S–H phases. Rather, chemical reactions above 700 °C are of great amplitude, and may be due to both calcite $CaCO_3$ decarboxylation and further C–S–H decomposition.

4.2. Mass loss after heat cycling

Sample mass has been measured before and after heat cycling, see Table 1. As explained above, mass variation is due to free water release up to 105/145 °C and C–S–H dehydration for higher temperatures. Initially, dry mortar sample No. 23 is reputed exempt of free pore water, yet its mass after heating cycles is significantly smaller than before. This means that bound water loss occurred during heating. On the opposite, for dry CEM V concrete sample, mass variation (expressed as a percentage of its initial mass) is very slight, with a 0.3% value only. Indeed, the dry CEMV concrete sample has been heated up to 200 °C for a shorter duration than dry mortar so that it had less time to release bound water, all the more so as bulk material releases water with more difficulty than powdered material as used for TGA analysis. TGA results may therefore be considered as upper bounds for structural water release amounts. As expected, partially-saturated samples all lose significant mass proportions, which may be a combination of free pore water and bound water release. After heating cycles, mortar samples have been stored at 105 °C for 4 weeks, so as to check for potential further mass loss. Mortar samples No. 23, No. 16, No. 17 and No. 26 lose respectively 0.22, 0.22, 0.27 and 0.16 g. Compared to their initial mass and mass loss after heat cycles, these slight variations can be neglected, which means that after heating cycles, no more free water may be released from the porous network.

4.3. Initial and residual transport properties

Apparent gas permeability K_{app} results are presented in Table 3. As expected, prior to heating, K_{app} values are greater for dry samples than for partially-saturated ones, and the higher the saturation rate, the lower the apparent gas permeability. Similarly, values of K_{app} after heating cycles are greater than before. This increase in K_{app} is attributed to free water drainage in the porous network, and later, to bound water drainage, rather than to micro-crack creation in the solid matrix during heating, because a significant confinement (around 5 MPa) has been kept constant throughout the tests, so that potential micro-cracks would have remained closed, see [21].

Finally, after heat cycling, gas permeability of all mortar samples, either initially dry or partially-saturated, is of the same order of magnitude (i.e. $2\times10^{-17}\,m^2$), which testifies (at least) of extensive free water removal from initially partially-saturated samples. A similar effect is observed for partially-saturated CEM V concrete sample: an order of magnitude in gas permeability is lost due to heat cycling.

4.4. Gas retention effect for mortar

4.4.1. Dry material

For initially dry sample No. 23, see Fig. 3(a), a clear permeability decrease is recorded from 146 °C and up to 200 °C, to such an extent that permeability K_{app} is almost divided by two at 200 °C; beyond 200 °C, K_{app} increases back again up to its initial value K_0. This phase lasts for 2 h 05 min. From then on, permeability passes beyond K_0 at stabilised temperature (ca. 206 °C). For such dry material, permeability decrease during heating cannot be due to free water inside the macropores. Rather, TGA results show that C–S–H dehydration (and/or ettringite decomposition) begins from 90 °C and potentially up to more than 240 °C. Therefore, bound water release inside the interconnected pore network is very probably the origin of gas flow slackening. Released bound water takes at least 2 h to get outside the sample through the gas flow, until permeability gets back to its initial value K_0, and gets even higher, due to microstructural modifications induced by this water release. To further assert this interpretation, water drainage is observed as water droplets at the gas pipe outlet from about 172 °C, see Fig. 4(a).

4.4.2. Water saturation effect

For both long partially-saturated samples No. 16 and No. 17, see Figs. 3(b) and 5(a), a clear decrease in permeability K_{app} is observed up to about 60 °C during the first 2 cycles (up to, respectively, 60 and 100 °C), so that K_{app} is divided down by two. Then permeability increases back again up to values higher than K_0, and the longer the cycle duration, the higher the final permeability value. This permeability decrease is attributed mainly to water dilation, so that pore passages get narrower, rather than to solid skeleton thermal deformations. Indeed, at such temperature levels, liquid water has not begun to vaporize. Moreover, liquid water has a linear thermal dilation coefficient α of about $2.6\times10^{-4}K^{-1}$, while, for cement paste, α is of 11×10^{-6} to $16\times10^{-6}K^{-1}$ and α for most aggregates ranges from 5×10^{-6} to $13\times10^{-6}K^{-1}$ [47]. Therefore, water dilation has a much stronger effect on pore passages to gas than solid skeleton thermal deformations.

Table 3
Apparent permeabilities before and after heating cycles, occurrence and duration of gas retention (or moisture clog) effect for each sample.

Sample	$K_0 = K_{app}$	K_{app}	Gas retention effect		
	Before heating	After heating cycles	T° begin	T° end	Duration
	(m^2)	(m^2)	(°C)	(°C)	
No. 23	1.8×10^{-17}	2.5×10^{-17}	None		
No. 16	2.7×10^{-18}	2.5×10^{-17}	181.6	210.8	2h19
No. 17	6.1×10^{-19}	2.1×10^{-17}	143.5	207.8	4h42
No. 26	4.0×10^{-18}	–	None		
CEMV No. 1	4.1×10^{-17}	6.2×10^{-17}	None		
CEMV No. 2	4.8×10^{-19}	5.1×10^{-18}	20.6	105.0	1h20

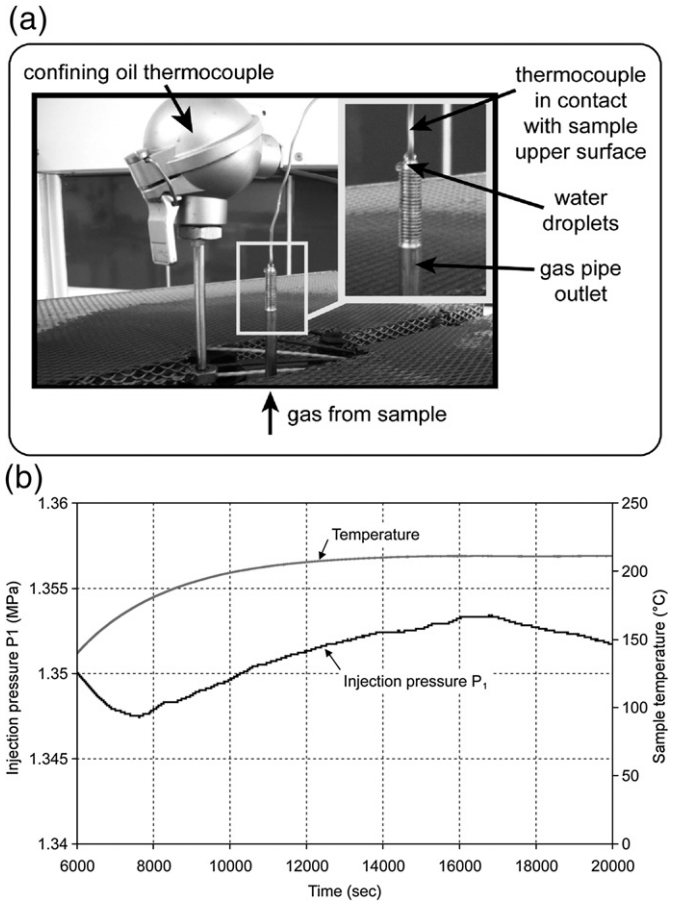

Fig. 4. Evidences of water vapour movements from the sample: (a) Water droplets are systematically observed at the gas pipe outlet, during heating; (b) Injection pressure P_1 increases with temperature for partially-saturated and long mortar sample No. 16.

Residual permeability after heating/cooling cycles up to 60 °C or 105 °C has also been evaluated. For all partially-saturated samples (Nos. 16, 17, 26 and even concrete CEM V No. 2), it is either higher or lower than K_0, i.e. residual permeability after 60 or 105 °C heat cycling does not display any clear trend. After such cycles, capillary water is still present inside the macro-pores, because cycle duration is relatively short (about 3 to 5 h each) and temperature levels are low. Our interpretation is that free water is not only partially released out of the sample, but, as water pressurizes when trying to dilate due to heating, it is also rearranged and redistributed inside the porous network, so that gas may have more or less easiness to pass it after heat cycling, i.e. residual gas permeability is either lower or higher than initially measured. Chemistry of the water pore solution might also be of influence when considering liquid water movements within the pore network, yet this effect has not been investigated in the present work.

Usually, all along a heating cycle, gas flows regularly throughout the sample, so that its injection pressure P_1 decreases regularly of ΔP during Δt, and permeability K_{app} may be deduced from Eqs. (2), (3) and (6). Instead, for long partially-saturated mortar samples Nos. 16 and 17, and during the third heating cycle (up to 200 °C), P_1 increases with temperature, see Fig. 4(b). For sample No. 16, this occurs from 181.6 °C and up to 210.8 °C and lasts for 2 h 19 min, see Table 3. This increase in P_1 means that no gas is able to pass the sample and gas permeability becomes zero, see Fig. 3(b). We are in the presence of a *gas retention phenomenon*, which is attributed to *moisture clogging*. Moisture clogging refers to hindered gas flow in presence of water

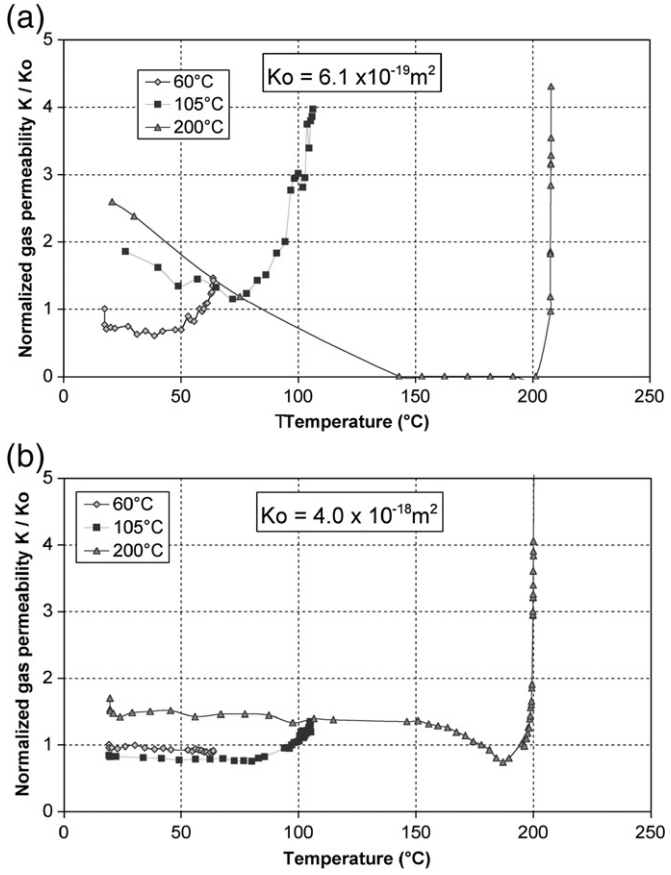

Fig. 5. Effect of sample size for partially-saturated mortar samples (a): long sample No. 17 (Sw = 53.4%); (b): Short sample No. 26 (Sw = 50.8%). Initial apparent gas permeability K_o is also given.

(liquid or vapour), so that it may be affected by both liquid content (i.e. initial water saturation level S_w) and water vapour formation above 100 °C. Indeed, not only do water droplets flow out of the set-up, see Fig. 4(a), but also water vapour (or liquid water) pushes gas out of the set-up on the upstream sample side. This is evidenced during the test when the upstream gas pipe is dismounted, because liquid water gets out of the pipe nipple situated at the cell base.

For sample No. 17, gas retention occurs more sharply than for sample No. 16, see Figs. 3(b) and 5(a). It is recorded from 143.5 °C and up to 207.8 °C, and lasts for 4 h 42 min, i.e. almost twice as long as for sample No. 16. Both observations are attributed to higher initial water saturation S_w for sample No. 17 than for sample No. 16, see Table 1.

For all partially-saturated samples, water droplets flow out of the downstream gas pipe at lower temperatures than for dry sample No. 23. Water droplets appear from 122 °C for long sample No. 16, from 142 °C for long sample No. 17 and from 128 °C for short sample No. 26. This is interpreted as being due to free water drainage and bound water drainage as well. Once this phenomenon has started, it lasts throughout the heating cycle (up to 200 °C).

4.4.3. Scale effect

For short and partially-saturated mortar sample No. 26, see Fig. 5(b), no gas retention phenomenon is observed. For sufficiently small samples, water vapour drainage occurs quickly enough so that gas transport is not affected dramatically. Such a diffusion mechanism as water vapour drainage out of a material porous network is acknowledged to vary, for a given duration, with the square of the specimen dimension l^2 along the main flow axis (here the vertical axis) [48]. Therefore, increasing the length-to-diameter ratio of our specimens by two multiplies diffusion time by four. This appears sufficient to slow water vapour diffusion so as to impede proper gas flow through the longer sample, see Fig. 5(a). We also note that for short and partially-saturated mortar sample No. 26, a permeability decrease occurs from 151 °C and up to 199 °C during the third heating cycle (up to 200 °C), and lasts for 1 h 53 min. In such instance, the sample is subjected to free water drainage (by vapour diffusion), but also to bound water release: the kinetics of both mechanisms combine, so that the gas passage through the pore network is partially hindered.

4.5. Permeability results and gas retention effect for concrete

Results are presented in Fig. 6(a) and (b). For dry CEM V No. 1 sample, gas permeability K_{app} does not change significantly during heating, even along the third heating cycle up to 200 °C. We also observe only a slight permeability variation before and after all three heating cycles, see Table 3. This accounts for a very good temperature resistance, attributable to a low bound water content of the C–S–H individually, together with a stronger water bond inside those C–S–H, thanks to fly ash and blast furnace slag presence.

For partially-saturated CEM V No. 2 concrete sample, gas permeability is divided by two as soon as during the first heating cycle up to 60 °C, and a gas retention phenomenon is recorded from the second heating cycle up to 105 °C only, from as low a temperature as 20.6 °C and up to 105 °C. This lasts for 1 h 20 min, see Fig. 6(b). Gas difficulties in passing through concrete are attributed mainly to free water dilation and/or flow out of the sample, because dry sample CEM V No.1 testing has shown that no major bound water release occurs up to 200 °C heating. Moreover, when gas retention is over after the second heating cycle, it does not occur anymore during the subsequent (and third) heating cycle. Therefore, gas retention occurs much quicker with CEM V concrete than with normalised mortar. This

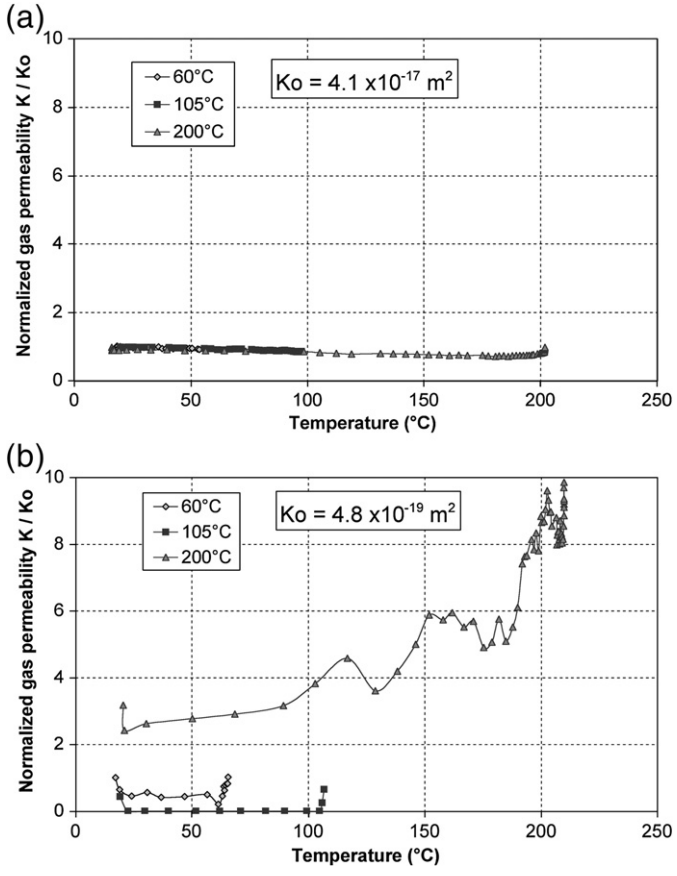

Fig. 6. (a): Dry concrete sample CEMV No. 1; (b): Partially-saturated concrete sample CEMV No. 2 (Sw = 79.6%). Initial apparent gas permeability K_o is also given.

is possibly mainly due to the very high sample initial saturation rate: $S_w = \approx 80\%$, for both material have similar porosities. During the third heating cycle, oscillations in K_{app} are attributed to free water vapour condensation and drainage at the downstream pipe side, for these occur at very close time intervals.

5. Conclusion

Using experimental evidence, this study has shown that a gas retention phenomenon could occur in cement-based materials subjected simultaneously to hydrostatic loading and to a *uniform* temperature up to 200 °C. This gas retention phenomenon depends mainly upon the applied heating rate (although the sample is continuously at uniform temperature all over its volume), the cement paste composition, the initial saturation level S_w, and it is also amplified by the sample scale. Gas retention phenomenon is attributed to water vapour (and/or liquid water) clogging the material porous network, so that gas becomes temporarily unable to pass through the specimen. This phenomenon has not been observed for initially dry materials, although, in such instances, gas permeability may be divided as much as down by two (mortar specimens). This is attributed to bound water release from the C–S–H. Gas retention phenomenon does not occur either for mortar samples of length-to-diameter ratios of about 1, for which gas or liquid evacuation from the porous network is easier (kinetic effect). In the extreme, gas retention is bound to occur for normalised mortar samples of height-to-diameter ratios of ca. 2, initial saturation rates S_w from around 45%, and heating rates from 2.5 to 4.9 °C/min.

The cement-based material composition also affects gas retention. Indeed, for CEMV concrete, and contrarily to normalised mortar, bound water release from the C–S–H spans over a wider temperature range due to the presence of additives such as fly ash and blast furnace slag which modify the C/S ratio of C–S–H. This is thought to explain the steadiness of CEMV concrete gas permeability with temperature when initially dry. Complementarily, as for normalised mortar, high initial saturation levels (ca. 80% and above) induce gas retention within CEMV concrete.

As for further prospects to this work, spatial temperature gradients have not been tackled here, since all samples are under uniform temperature all along heat cycling. However, this could worsen gas retention effects and even induce additional physical phenomena which could not be observed here. Another potentially influential effect is that of material porosity, yet this was not be studied here because both mortar and concrete display similar porosities (12.9 and 14.2% respectively). Moreover, due to the high hydrostatic pressure applied in the experiments ($P_c = 5$ MPa), micro-cracking due to heat cycling is likely to have been greatly reduced. In practice, however, microcracking would be bound to occur. These aspects will be tackled in further work.

Acknowledgments

The authors are grateful to Th. Dubois for technical expertise, and to Ms. Flore Brue for CEM V concrete porosity measurements. EDF and ANDRA are also warmly acknowledged for financial support.

References

[1] Z.P. Bažant, M.F. Kaplan, Concrete at high temperatures: material properties and mathematical models, Longman Group, England, 1996.
[2] F.J. Ulm, O. Coussy, Z.P. Bažant, The 'Chunnel' fire. I. Chemoplastic softening in rapidly heated concrete, Journal of Engineering Mechanics 125 (3) (1999) 272–282.
[3] Z.P. Bažant, Analysis of pore pressure, thermal stress and fracture in rapidly heated concrete, Proceedings of International Workshop on Fire Performance of High-Strength Concrete, Nation Institute of Standards and Technology, Gaithersburg, Md, 1997, pp. 155–164.
[4] S. Dal Pont, A. Ehrlacher, Numerical and experimental analysis of chemical dehydration, heat and mass transfers in a concrete hollow cylinder submitted to high temperatures, International Journal of Heat and Mass Transfert 47 (2004) 135–147.
[5] S. Dal Pont, S. Durand, B.A. Schrefler, A multi-phase thermo-hydro-mechanical model for concrete at high temperatures — Finite element implementation and validation under LOCA load, Nuclear Engineering and Design 237 (2007) 2137–2150.
[6] C. Davy, F. Skoczylas, J.-D. Barnichon, P. Lebon, Permeability of macro-cracked argillite under confinement: gas and water testing, Physics and Chemistry of the Earth 32 (2007) 667–680.
[7] F.J. Ulm, P. Acker, M. Lévy, The 'Chunnel' fire. II. Analysis of concrete damage, Journal of Engineering Mechanics 125 (3) (1999) 283–289.
[8] G.F. Peng. *Evaluation of fire damage to high performance concrete*. PhD thesis, The Hong Kong Polytechnic University, Hong Kong, 1999.
[9] L.T. Phan, Fire performance of high-strength concrete: A report of the state-of-the art. Technical Report NIST I.R. 5934, Nation Institute of Standards and Technology (NIST, Gaithersburg, Md, 1997.
[10] Y. Msaad, G. Bonnet, Analyses of heated concrete spalling due to restrained thermal dilation: application to the 'Chunnel' fire, Journal of Engineering Mechanics 132 (10) (2006) 1124–1132.
[11] Y. Msaad, Comparison between hydraulic and thermal spalling in heated concrete based on numerical modeling, Journal of Engineering Mechanics 133 (6) (2007) 608–615.
[12] X.T. Chen, J.F. Shao, C.A. Davy, and F. Skoczylas. Experimental study and elastoplastic damage modeling of mortar with thermal effects. submitted to the International Journal for Numerical and Analytical Methods in Geomechanics, 2008.
[13] Y.F. Fu, Y.L. Wong, C.A. Tang, C.S. Poon, Thermal induced stress and associated cracking in cement-based composite at elevated temperatures-part II: thermal cracking around multiple inclusions, Cement and Concrete Composites 26 (2004) 113–126.
[14] X.T. Chen, C.A. Davy, F. Skoczylas, J.F. Shao, Effect of heat-treatment and hydrostatic loading upon the poro-elastic properties of a mortar, Cement and Concrete Research 39 (2009) 195–205.
[15] T.Z. Harmathy, Effect of moisture on the fire endurance of building materials, ASTM Special Technical Publication, Philadelphia, STP 385 (1965) 74–95.
[16] Y. Anderberg, Spalling phenomena of HPC and OC, Proceedings of International Workshop on Fire Performance of High-Strength Concrete, Nation Institute of Standards and Technology, Gaithersburg, Md, 1997, pp. 69–73.
[17] P. Kalifa, F.D. Menneteau, D. Quenard, Spalling and pore pressure in HPC at high temperatures, Cement and Concrete Research 30 (2000) 1915–1927.
[18] K.J. Willam, E.P. Warnke, Constitutive model for the triaxial behaviour of concrete, IABSE Proc., 19-Seminar on Concrete Structures Subjected to Triaxial Stresses, Assoc. for Bridge and Structural Engineering, Zurich, Switzerland, 1975, pp. III–1.
[19] C. Davy, F. Skoczylas, P. Lebon, Th. Dubois, Gas migration properties through a bentonite/argillite interface, Applied Clay Science 42 (2009) 639–648.
[20] P. Mounanga. Etude expérimentale du comportement de pâtes de ciment au très jeune âge : hydratation, retraits, propriétés thermophysiques. In *Thèse de doctorat de l'Université de Nantes (PhD Thesis, in French)*, 2003.
[21] M. Lion, F. Skoczylas, Z. Lafhaj, M. Sersar, Experimental study on a mortar. Temperature effects on porosity and permeability. Residual properties or direct measurements under temperature, Cement and Concrete Research 35 (2005) 1937–1942.
[22] M.C.R. Farage, J. Sercombe, C. Gallé, Rehydration and microstructure of cement paste after heating at temperatures up to 300 C, Cement and Concrete Research 33 (2003) 1047–1056.
[23] Y.F. Fu, Y.L. Wong, C.S. Poon, C.A. Tang, P. Lin, Experimental study of micro/macro crack development and stress–strain relations of cement-based composite materials at elevated temperatures, Cement and Concrete Research 34 (2004) 789–797.
[24] X.T. Chen, W. Chen, C.A. Davy, F. Agostini, F. Skoczylas, Gas retention phenomenon in dry or partially-saturated concrete: permeability assessment, Thermo-Hydro-mechanical and Chemical Coupling in Geomaterials and Applications , Proceedings of the 3rd International Symposium GeoProc 2008, J. Wiley & Sons, New York, 2008, pp. 151–159.
[25] H.W. Reinhardt, M. Jooss, Permeability and self-healing of cracked concrete as a function of temperature and crack width, Cement and Concrete Research 33 (2003) 981–985.
[26] M. Choinska. *Effets de la température, du chargement mécanique et de leurs interactions sur la perméabilité du béton de structure*. Thèse de Doctorat (PhD Thesis, *in French*), Ecole Centrale de Nantes/Université de Nantes, France, 2006.
[27] L. Montigny. Perméabilité au gaz de bétons sous haute température. Master's Thesis (in French), Ecole Centrale de Lille, France, 2006.
[28] Y. Benachour, C.A. Davy, F. Skoczylas, H. Houari, Effect of a high calcite filler addition upon microstructural, mechanical, shrinkage and transport properties of a mortar, Cement Concrete Research 38 (2008) 727–736.
[29] D.R. Lide (Ed.), CRC Handbook of Chemistry and Physics, 82nd Ed, CRC Press, Boca Raton, FL, 2001.
[30] E. Dana, F. Skoczylas, Experimental study of two-phase flow in three sandstones. II. capillary pressure curve measurement and relative permeability pore space capillary models, International Journal of Multiphase Flow 28 (12) (2002) 1965–1981.
[31] I. Yurtdas, N. Burlion, F. Skoczylas, Experimental characterization of the drying effect on uniaxial mechanical behaviour of mortar, Materials and Structure 37 (267) (2004) 170–176.
[32] I. Yurtdas, N. Burlion, F. Skoczylas, Triaxial mechanical behaviour of mortar: effects of drying, Cement and Concrete Research 34 (2004) 1131–1143.
[33] N. Burlion, D. Bernard, D. Chen, X-ray microtomography: application to microstructure analysis of a cementitious material during leaching process, Cement Concrete Research 36 (2006) 346–357.
[34] I. Yurtdas, H. Peng, N. Burlion, F. Skoczylas, Influences of water to cement ratio on mechanical properties of mortars submitted to drying, Cement and Concrete Research 36 (2006) 1286–1293.
[35] F. Skoczylas, N. Burlion, I. Yurtdas, About drying effects and poro-mechanical behaviour of mortars, Cement Concrete Composites 29 (2007) 383–390.

[36] F.J. Ulm, G. Constantinides, F.H. Heukamp, Is concrete a poromechanics materials? A multiscale investigation of poroelastic properties, Materials and Structures/ Concrete Science and Engineering 37 (2004) 43–58.
[37] P. Lebon, B. Mouroux, Knowledge of the three French underground laboratory sites, Engineering Geology 52 (1999) 251–256.
[38] T. Hastié, R. Tibshirani, J. Friedman, The Elements of Statistical Learning: Data Mining, Influence and Prediction, In Springer, NY, 2003.
[39] F. Lea, The Chemistry of Cement and Concrete, J.Wiley & Sons Ed, 1998.
[40] M. Castellote, C. Alonso, C. Andrade, X. Turrillas, Composition and microstructural changes of cement pastes upon heating, as studied by neutron diffraction, Cement Concrete Research 34 (2004) 1633–1644.
[41] B.A. Clark, P.W. Brown, The formation of calcium sulfoaluminate hydrate compounds: part I, Cement & Concrete Research 29 (1999) 1943–1948.
[42] B.A. Clark, P.W. Brown, The formation of calcium sulfoaluminate hydrate compounds: part ii, Cement & Concrete Research 30 (2000) 233–240.
[43] V. Baroghel-Bouny. *Caractérisation microstructurale et hydrique des pâtes de ciment et des bétons ordinaires et à très hautes performances*. Thèse de Doctorat (PhD Thesis, *in French*), Ecole Nationale des Ponts et Chaussées, Paris, 1994.
[44] K. Fuji, W. Kondo, Heterogeneous equilibrium of calcium silicate hydrate in water at 30 °C, Journal of the Chemical Society. Dalton Transactions 2 (1981) 645–651.
[45] I.G. Richardson, The nature of the hydration products in hardened cement pastes, Cement & Concrete Composites 22 (2000) 97–113.
[46] I.G. Richardson, The calcium silicate hydrates, Cement & Concrete Research 38 (2008) 137–158.
[47] A.M. Neville, Properties of Concrete, 4th EdWiley & Sons, 1996.
[48] E. Guyon, J.P. Hulon, L. Petit, P.-G. de Gennes, Hydrodynamique physique, EDP Sciences, CNRS Editions, 2001.